



1  
2  
3  
4  
5  
6  
7  
8  
9  
10  
11  
12  
13  
14  
15  
16  
17  
18  
19  
20  
21  
22  
23  
24  
25  
26  
27  
28  
29  
30  
31  
32  
33  
34  
35  
36  
37  
38  
39  
40  
41  
42  
43  
44  
45

## Celestial Mechanics and Estimating the Termination of the Holocene

**John A. Parmentola**

The RAND Corporation

1776 Main Street

Santa Monica, CA 90401 USA

Email address: [johnparmentola@gmail.com](mailto:johnparmentola@gmail.com)

### Abstract

This paper addresses several issues concerning Milankovitch Theory and its relationship to paleoclimate data over the last 800,000 years. A model is presented that deconvolutes the precession index (precession modulated by the eccentricity) and the obliquity contributions to the percentage change between successive mean-daily-insolation minima and maxima. The sum of these contributions is in close agreement with the corresponding benchmark calculation of J. Laskar et al. The model predictions indicate that the precession index contribution dominates such insolation changes, and its time-dependent behavior correlates with the occurrence of interglacial and glacial periods and temperature trends during these periods. Best fit curves to the separate contributions appear as quasiperiodic waves that correlate with interglacial initiations and terminations through their constructive and destructive interference. However, a comparison of model predictions with the EPICA Dome C (EDC) data indicates delayed inceptions for Marine Isotope Stages 18d and 13c, which have also been noted by Parrenin et al. through a comparison of LR04 benthic  $\delta^{18}\text{O}$  and EDC ice core datasets. Finally, the model enables the classification of interglacial periods into two distinct types that approximately account for their durations. This classification also enables a low-resolution estimation of the Holocene termination based solely on celestial mechanical forcing.

### I. Introduction

Since Milutin Milankovitch's seminal papers (Milankovitch, 1998) concerning the occurrence of ice ages, numerous papers have supported (Hays et al., 1976; Imbrie, 1982; Imbrie et al., 1986; Zachos et al., 2001; Gradstein et al., 2005; Huybers et al., 2011; Roe, 2006) and challenged (Wunsch, 2004; Berger, 2011) his hypothesis that changes in insolation at northern latitudes during the summer solstice is the likely cause of ice sheet changes associated with ice age occurrences. A substantial number of papers have connected eccentricity, precession, and obliquity cyclical behaviors to features in the paleoclimate data (Lisiecki et al., 2005; Lisiecki, 2010). For example, these celestial parameters, as well as the insolation, exhibit specific characteristic frequencies that are also found in spectral analyses of paleoclimate data over the Pleistocene (Meyers et al., 2008). However, this approach does not completely account for interglacial and glacial durations and the timing of the prominent temperature excursions in paleoclimate data, such as those exhibited in EDC ice core data and other datasets (NCEI, 2007; Jouzel, 2013).



46 In his original papers (Milankovitch, 1998), Milankovitch proposed that the obliquity  
47 played a dominant role in ice age occurrences because it affects the insolation at northern  
48 latitudes where ice and snow can accumulate on the earth's comparatively large landmass.  
49 However, this hypothesis is still unproven, and the quantitative roles of the eccentricity and  
50 precession in the earth's paleoclimate history remain an active area of research (Lisiecki, 2010).  
51 Consequently, the eccentricity, precession, and obliquity contributions to the insolation and their  
52 correlation with paleoclimate data remain uncertain.

53

54 Finally, the behaviors of these three celestial parameters have been used to identify past  
55 interglacial periods like the Holocene (Vavrus et al., 2018; Berger et al., 2003; Rohling et al.,  
56 2010). This form of pattern recognition has enabled quantitative estimates of the Holocene  
57 termination. However, such estimates would be much more convincing if the conditions of the  
58 Holocene termination due to celestial mechanical forcing coincided with all other past  
59 interglacial terminations.

60

61 The new results presented here clarify these issues. The provisional assumption is that the  
62 percentage change between successive mean-daily-insolation maxima and minima (insolation  
63 half-cycles) significantly influenced the timing and duration of prominent features in  
64 paleoclimate data, such as the major temperature excursions in the EDC ice core data and other  
65 datasets (NCEI, 2007; Jouzel, 2013). This assumption has the added advantage that the  
66 precession index and obliquity contributions to the percentage change between successive mean-  
67 daily-insolation maxima and minima can be deconvoluted quantitatively. This separation enables  
68 insight into their cyclical behaviors and amplifying, and dampening effects on the insolation over  
69 extended periods. As it turns out, both contributions are quasiperiodic, which is a consequence  
70 of the aperiodic nature of the earth's eccentricity, precession, and obliquity. However, their  
71 cyclical behaviors differ from these celestial parameters. This cyclical complexity and their  
72 individual insolation behaviors approximately correlate with prominent EDC ice core data  
73 features.

74

75 Section II briefly describes the basic assumption and emphasizes the quasiperiodic  
76 eccentricity, precession, and obliquity behaviors. Section III presents a deconvolution model  
77 along with its predictions for the obliquity and precession index contributions to the percentage  
78 change between successive mean-daily-insolation extrema. The sum of these contributions is  
79 compared with the corresponding theoretical calculations of J. Laskar et al. (IMCCE, 2018;  
80 Laskar et al., 2004). Comparisons are also made between the aperiodic behaviors of the three  
81 celestial parameters and those of the precession index and obliquity contributions to the  
82 percentage change between successive insolation extrema. In Section IV, the model predictions  
83 are compared with the EDC dataset. Timing discrepancies between the EDC data and the model  
84 are identified; however, evidence is presented that suggests the model predictions could be  
85 correct. In Section V, a low-resolution estimate for the Holocene termination is presented. A  
86 possible physical mechanism within the earth's climate system is also proposed to account for  
87 the significant declines in temperature associated with ice ages; however, this proposal is a  
88 conjecture requiring further research. In Section VI, the agreement between the data and the  
89 model, as well as timing discrepancies and their suggested resolution, are summarized.

90

91



92

93

## II. Background

94

95

The sun's solar irradiance is a persistent effect on the earth's atmosphere distributed over its surface (the insolation) through its shape and quasiperiodic celestial mechanical motions. These motions cause the insolation at a latitude to oscillate in an aperiodic manner about an average value. Its magnitude varies depending on the earth's distance from the sun, the direction the earth's axis points, and its tilt angle.

100

101

The main point of this paper is to provide insight into the insolation's time-dependent behavior through its separation into precession index and obliquity contributions. This separation reveals that the precession index contribution amplifies and reduces the insolation while the obliquity is a much smaller and narrowly bound contribution to the insolation. Both quasiperiodic behaviors are shown to correlate with the prominent features in paleoclimate data over the last 800,000 years.

106

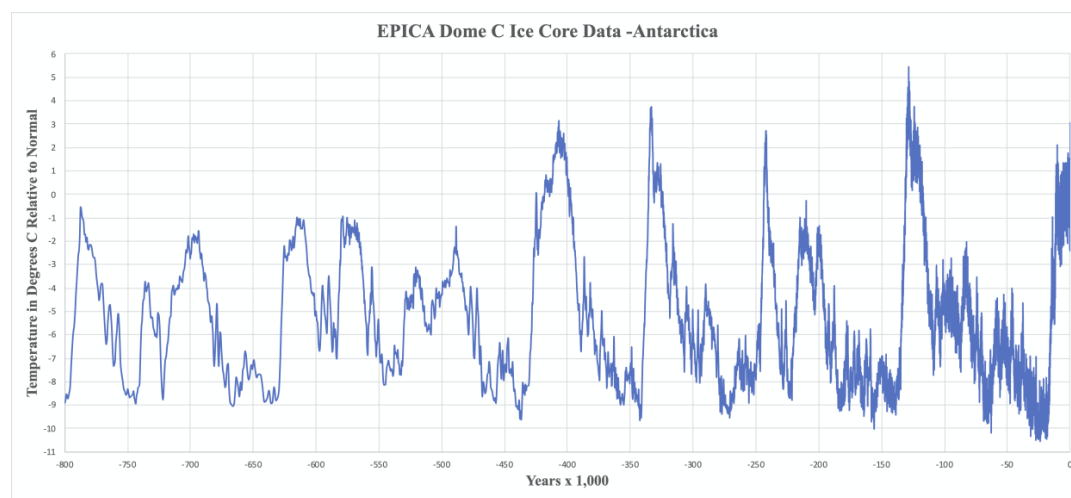
107

108

This paper assumes the percentage change between successive mean-daily-insolation maxima and minima at 65 degrees northern (65N) latitude during the summer solstice (June) over the last 800,000 years, substantially influenced the prominent features in paleoclimate data such as the EDC dataset depicted in Figure 1,

111

112



113

114

Figure 1. EDC ice core data based on a temperature reconstruction model using deuterium as a proxy presented in degrees centigrade relative to normal from -800,000 years to the present (NCEI, 2007).

115

116

Figure 1 is a temperature reconstruction from ice core data using deuterium as a proxy; however, it's model-dependent. Physical effects can affect the dating of temperature changes inferred from ice cores. As discussed in Section IV, such effects become evident when deconvolution model predictions are compared to the EDC ice core data.

120

121

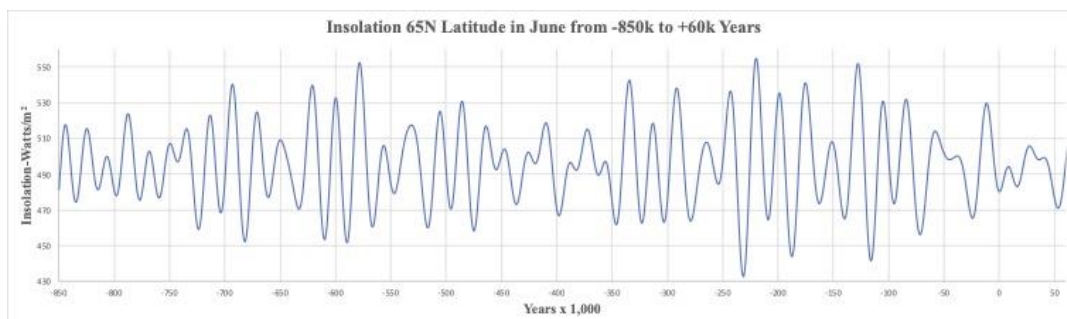
122

Over the last 800,000 years, the mean-daily-insolation at 65N latitude during June underwent 74 transitions between successive maxima and minima, as indicated in Figure 2,

123



124



125

126

127

Figure 2. Mean-daily-insolation at 65N latitude in June for the period -850,000 to +60,000 years (IMCCE, 2018).

128

129

130

These transitions range in percentage from about 28% to -19% (in some cases exceeding 100 Watts/m<sup>2</sup> in magnitude) with half-cycle durations (the average is about 11,000 years) that range from 4,200 to 16,900 years.

131

132

133

134

135

136

137

138

Reconciling the 74 transitions of Figure 2 in terms of timing and amplitude with the prominent temperature excursions in Figure 1 is a formidable theoretical challenge. These features are affected by eccentricity, precession, and obliquity cyclical behaviors, which have been computed from -250 million to +250 million years (IMCCE, 2018; Laskar et al., 2004). According to the Milankovitch hypothesis, their determination provides a consistent temporal calibration that should correlate insolation changes with features in the paleoclimate data.

139

140

141

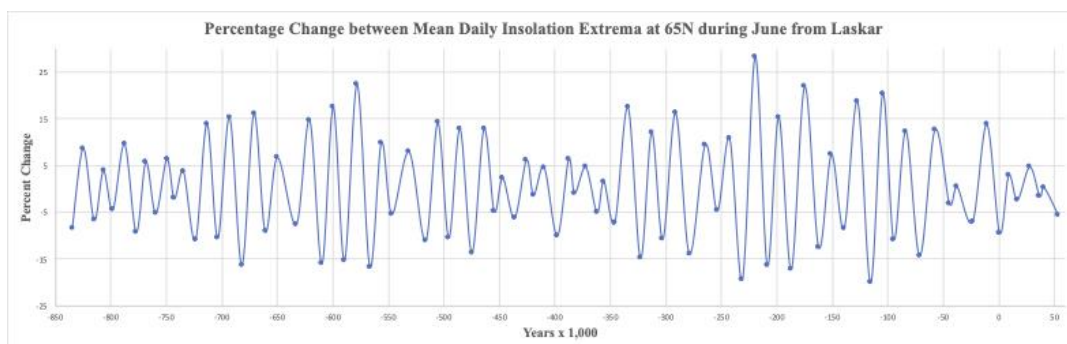
142

143

144

145

There has been considerable discussion in the literature concerning the cyclical durations of the eccentricity, precession, and obliquity and their correlation with various paleoclimate proxy data (Lisiecki et al., 2005; Lisiecki, 2010; Meyers et al., 2008). However, these durations correspond to frequencies of spectral power density maxima, which can obfuscate their complex individual aperiodic behaviors. These complex cyclical behaviors affect the percentage change between successive insolation maxima and minima that is represented in Figure 3,



146

147

148

149

Figure 3. Percentage change between successive mean-daily-insolation maxima and minima at 65N latitude in June during -844,200 to +53,500 years (IMCCE, 2018).

150

151

Note, the blue curve in Figure 3 is the best fit to a sparse set of points from -844,200 years to +53,500 years that should not be trusted for numerical precision between these points. However,



152 the timing accuracy of extrema percentage changes and the qualitative behaviors between these  
 153 points will be utilized to interpret paleoclimate data.

154

155 As will be demonstrated, the complex “beat structure” in Figure 3 is a result of the  
 156 superposition of recurring precession index wave packets (formed from a precession “carrier  
 157 wave” that is amplitude modulated by the eccentricity) and obliquity wave contributions to the  
 158 percentage change between successive mean-daily-insolation extrema. However, the half-cycle  
 159 durations of the precession carrier and obliquity wave contributions are shown in Section III to  
 160 be significantly different from the half-cycle durations of the three celestial parameters.  
 161 Nevertheless, the recurring precession index wave packets will be shown to correlate with  
 162 temperature trends in the EDC dataset and the recurrence of interglacial and glacial periods in  
 163 Section IV. It is also shown that the obliquity wave contribution correlates with the temperature  
 164 excursions in the paleoclimate data; however, there are timing differences between the obliquity  
 165 wave and the temperature excursions. These timing differences are ameliorated through the  
 166 constructive and destructive interference of the recurring precession index wave packets with the  
 167 obliquity wave.

168

### 169 **III. The Deconvolution Model**

170

171 This section separates the fractional change between successive mean-daily-insolation  
 172 maxima and minima into precession index and obliquity contributions. This separation is  
 173 accomplished, in part, through an application of the computational tool developed by J. Laskar et  
 174 al. (IMCCE, 2018; Laskar et al., 2004). The sum of these estimated contributions will be  
 175 compared to Laskar’s prediction. In what follows, the eccentricity, precession, obliquity, and  
 176 insolation parameters are specified with a temporal resolution of 100 years using Laskar’s tool.

177

178 The insolation,  $Q$ , is assumed to be of the form,

179

$$180 \quad Q = A \cdot B \quad (1)$$

181

182 , where  $A$  and  $B$  are respectively the precession index and obliquity contributions to the  
 183 insolation. In Appendix A,  $B$  is shown to depend on latitude and the sun’s declination angle.  
 184 Because daylight hours depend on latitude and the sun’s declination angle, the mean-daily-  
 185 insolation,  $\bar{Q}$ , is dependent on the mean-daily-obliquity contribution,  $\bar{B}$ . By averaging equation  
 186 (1) over daylight hours, the mean-daily-insolation is given by

187

$$188 \quad \bar{Q} = A \cdot \bar{B} \quad (2)$$

189

190 It’s straightforward to show from equation (2) that the fractional change in  $\bar{Q}$  produced through  
 191 changes in  $A$  and  $\bar{B}$  is approximately given by

192

$$193 \quad \frac{\Delta \bar{Q}}{\bar{Q}_i} \cong \frac{\Delta A}{A_i} + \frac{\Delta \bar{B}}{\bar{B}_i} \quad (3)$$

194



195 , where  $\frac{\Delta A}{A_i}$  and  $\frac{\Delta \bar{B}}{\bar{B}_i}$  are respectively the fractional precession index and obliquity contributions to  
196 the fractional change in the mean-daily-insolation,  $\frac{\Delta \bar{Q}}{\bar{Q}_i}$ , with  $\Delta \bar{Q} = \bar{Q}_f - \bar{Q}_i$ ,  $\Delta A = A_f -$   
197  $A_i$ , and  $\Delta \bar{B} = \bar{B}_f - \bar{B}_i$  are the respective changes in the mean-daily-insolation, and the  
198 precession index and obliquity contributions to the mean-daily-insolation with the subscripts,  $i$   
199 and  $f$ , designating the initial and final states. The correction cross-term,  $\frac{\Delta A}{A_i} \cdot \frac{\Delta \bar{B}}{\bar{B}_i}$ , to equation (3)  
200 will be shown to be negligible.

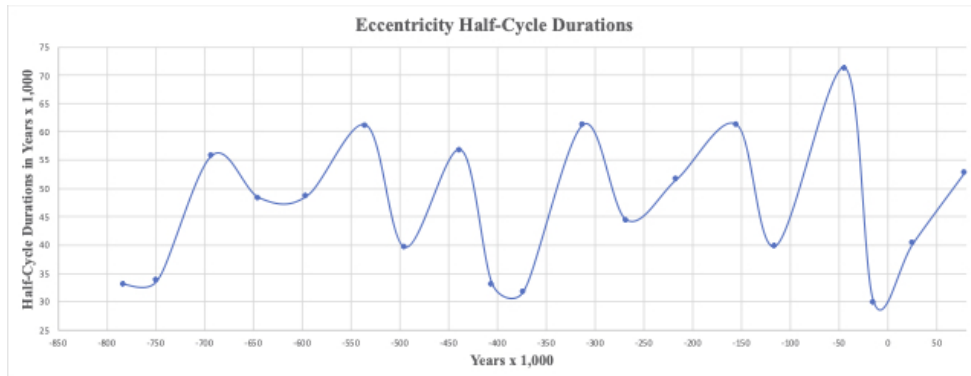
201

### 202 III.1 Precession Index Contribution

203

204 The earth's eccentricity has varied by more than an order of magnitude from about 0.004  
205 to 0.05 during the last 800,000 years. While the eccentricity is cyclical, it's not periodic. In terms  
206 of timescales, its average half-cycle duration has been about 47,000 years; however, this duration  
207 has varied between about 30,000 to 71,000 years, as indicated in Figure 4,  
208

209



210

Figure 4. Eccentricity half-cycle durations during the period -815,000 to +79,000 years (IMCCE, 2018).

211

212 The key to understanding the eccentricity's effect on the insolation at northern latitudes  
213 during the summer solstice is its change from the time the earth's axis points toward the sun at  
214 perihelion to the time it points toward the sun at aphelion. While the timescale of the precession  
215 index contribution to the insolation is affected by the eccentricity, its short-term half-cycle is  
216 primarily due to the precession. The average precession half-cycle duration has been about  
217 11,000 years; however, precession half-cycle durations have varied between about 7,000 to  
218 15,000 years, as indicated by the following graph,  
219

219

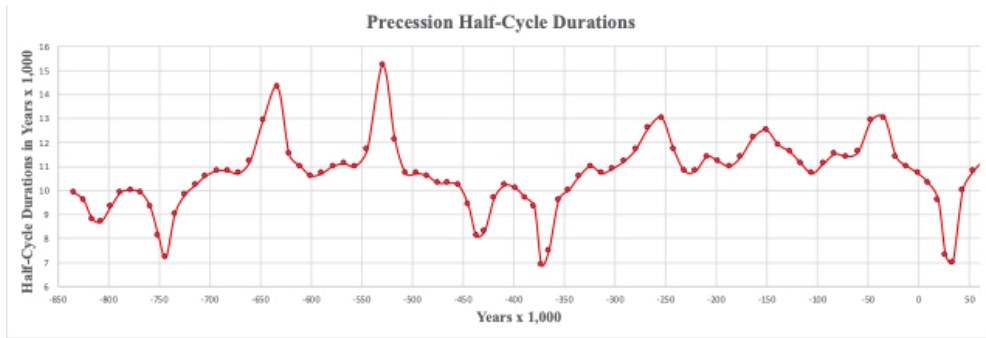


Figure 5. Precession half-cycle durations during the period -843,900 years to +54,200 (IMCCE, 2018).

220

221

222

223

224

225

226

227

228

229

230

231

232

233

234

235

236

237

238

239

240

241

242

243

244

245

246

247

248

249

250

251

The relatively small eccentricity changes over these precession half-cycles enable the approximate determination of the precession index contribution to the fractional change between mean-daily-insolation extrema. As discussed further below, the precession index contribution to the percentage change between successive insolation extrema at 65N during June takes the form of a quasiperiodic wave; however, its half-cycle durations differ from those of the precession.

Assuming the insolation depends on the inverse distance squared from the sun multiplied by an overall constant, the fractional change of the precession index contribution during a perihelion to aphelion half-cycle transition is given by

$$\frac{\Delta A_{p \rightarrow a}}{A_p} = \frac{(1 - e_p)^2}{(1 + e_a)^2} - 1 \quad (4)$$

, where the perihelion subscript,  $p$ , and aphelion subscript,  $a$ , are the initial and final states, respectively. Equation (4) is well approximated by

$$\frac{\Delta A_{p \rightarrow a}}{A_a} \approx -2(e_a + e_p) + e_p^2 + 4e_a e_p + 3e_a^2 \quad (5)$$

, where the linear term dominates. Similarly, in transitioning from aphelion to perihelion, the corresponding fractional precession index contribution is given by

$$\frac{\Delta A_{a \rightarrow p}}{A_a} = \frac{(1 + e_a)^2}{(1 - e_p)^2} - 1 \quad (6)$$

, which is also well approximated by

$$\frac{\Delta A_{a \rightarrow p}}{A_a} \approx 2(e_a + e_p) + e_a^2 + 4e_a e_p + 3e_p^2 \quad (7)$$

, where again the first term dominates, and the subscripts have corresponding interpretations. The eccentricity,  $e$ , depends on time and, in what follows, is specified by Laskar's tool at the time of each mean-daily-insolation maximum and minimum during June at 65N latitude.



252

253

254

255

256

257

258

259

260

261

262

263

264

265

266

267

268

269

270

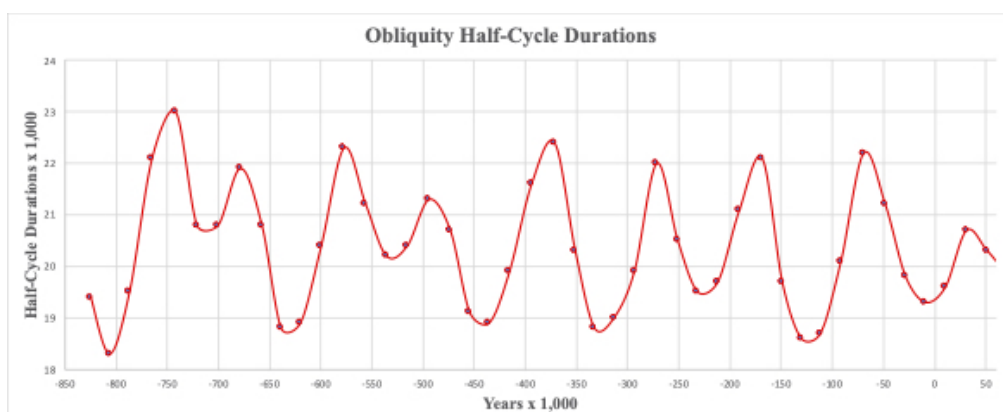
271

272

In deriving equations (4) and (6), the earth-sun distances at perihelion,  $R_p = a \cdot (1 - e_p)$ , and aphelion,  $R_a = a \cdot (1 + e_a)$ , are used, where,  $a$ , is the semi-major axis of the earth's orbit. The semi-major axis is assumed constant during an insolation transition between successive extrema, which implies eccentricity changes result from changes in the semi-minor axis. Also, because the eccentricity is a slowly varying function of time, differences in the time specification of insolation extrema and when the earth's axis successively points toward the sun at perihelion and aphelion and vice versa have a comparatively small impact on the insolation. This assessment is consistent with the comparison of deconvolution model results for the percentage change between successive insolation extrema at 65N during June as indicated in Figure 7 and the error analysis in Figure 8 below.

### III.2 Obliquity Contribution

The obliquity involves small angular changes ranging from a minimum of 22.1 to a maximum of 24.5 or 2.4 degrees. Because the obliquity oscillates about an average angle, its contribution to the insolation at a given latitude is also in the form of a quasiperiodic wave. The average obliquity half-cycle duration has been about 20,000 years over the last 850,000 years; however, it has ranged from approximately 18,000 to 23,000 years, as indicated in Figure 6,



273

274

275

**Figure 6.** Obliquity half-cycle durations during the period -844,700 years to +51,100 years (IMCCE, 2018).

276

277

278

279

280

281

282

283

284

285

The comparatively small and gradual change in the earth's tilt angle also enables the approximate determination of the obliquity contribution to the fractional change between successive mean-daily-insolation extrema. As discussed further below, the half-cycle durations of the obliquity contribution to the percentage change between insolation extrema differ from those of the obliquity.

By specializing to the summer solstice (the sun's declination angle equals the obliquity angle), in Appendix A, the fractional obliquity contribution to successive mean daily insolation during June is shown to be of the form,





286 
$$\frac{\Delta \bar{B}}{\bar{B}_i} = \frac{h_f \cdot \sin \phi \cdot \sin \theta_f + \cos \phi \cdot \cos \theta_f \cdot \sin h_f}{h_i \cdot \sin \phi \cdot \sin \theta_i + \cos \phi \cdot \cos \theta_i \cdot \sin h_i} - 1$$
 (8)

287  
288 , where  $\phi$  is the latitude = 1.134 radians or 65N, and  $\theta_i$  and  $\theta_f$  are the initial and final  
289 obliquity angles specified in radians with  $h_i$  and  $h_f$  the initial and final hour angles determined  
290 by,

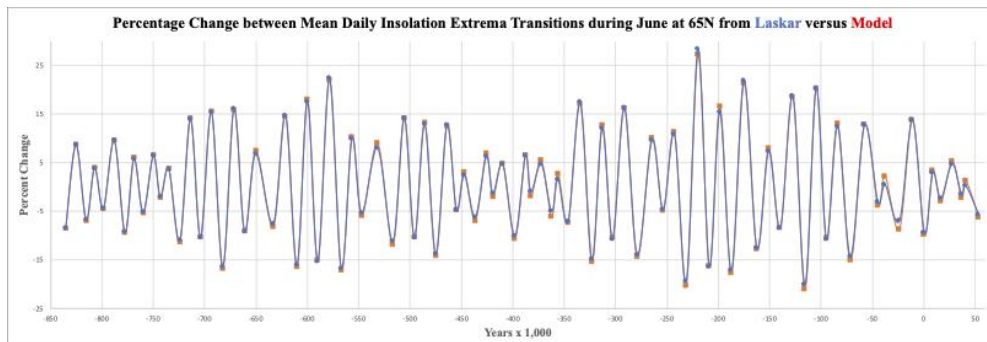
291 
$$h_j = \cos^{-1}(-\tan \phi \cdot \tan \theta_j)$$
 (9)

292  
293  
294 , which is also in radians. The obliquity range,  $0.386 \leq \theta \leq 0.428$  radians, implies a maximum  
295 percentage obliquity contribution to successive mean-daily-insolation extrema during June at  
296 65N latitude is about 8.6% from equations (8) and (9); however, this maximum is never realized  
297 (see further discussion below). In what follows, the obliquity angle,  $\theta$ , is specified by Laskar's  
298 tool at the time of each mean-daily-insolation maximum and minimum at 65N latitude during  
299 June. For successive insolation extrema transitions, equations (8) and (9) are surprisingly well  
300 approximated by

301  
302 
$$\frac{\Delta \bar{B}}{\bar{B}_i} \approx 2 \cdot (\theta_f - \theta_i)$$
 (10)

303  
304 The linear terms in equations (5), (7), and (10) can be used to provide reasonable “back  
305 of the envelope” estimates for the fractional change between successive mean-daily-insolation  
306 extrema at 65N latitude during June. However, in what follows, the more accurate  
307 deconvolution model predictions are utilized by substituting equations (4), (6), (8), and (9) into  
308 equation (3) to compare the model predictions with the corresponding Laskar predictions of  
309 Figure 3. This comparison is shown in Figure 7,

310



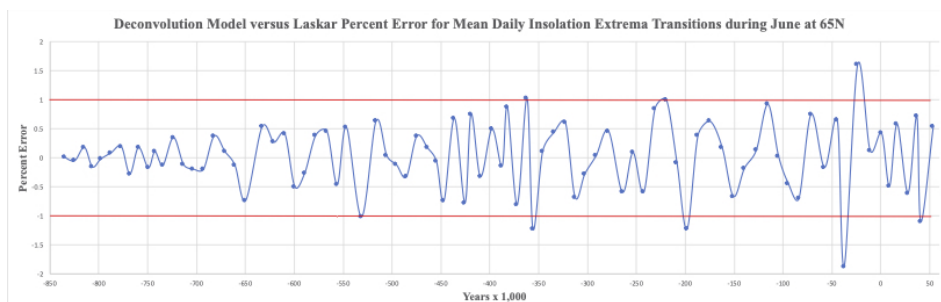
311  
312 Figure 7. Comparison of the deconvolution model approximation to the percentage change between successive  
313 mean-daily-insolation extrema at 65N latitude in June with the predictions of J. Laskar et al. in Figure 3.

314  
315 In Figure 7, the blue dots follow from Figure 3, and the red dots are deconvolution model  
316 estimates for the percentage change between successive mean-daily-insolation extrema at 65N  
317 latitude during June. A point wise error analysis of Figure 7 is represented in Figure 8,

318



319



320

321

322

323

324

325

326

327

328

329

330

331

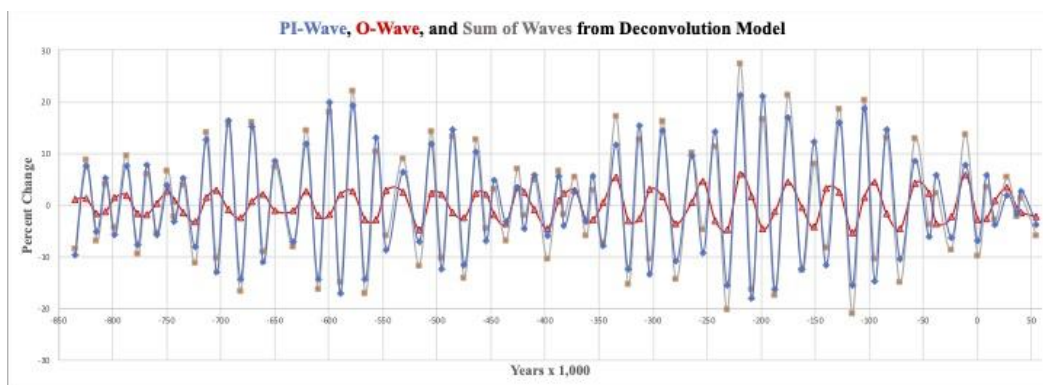
Figure 8. An analysis of Figure 7 indicates a + or -1% error bound on most points (horizontal red lines) with several points between + or -1 and + or -2%.

For most points, the error is bounded by + or -1%. The comparatively few exceptions are of no consequence to the analysis presented below.

The complex “beat structure” in Figure 7 results from the superposition of the precession index and obliquity contributions to the percentage change between successive mean-daily-insolation extrema, which follow from equations (4), (6), (8), and (9) and are represented in Figure 9,

332

333



334

335

336

337

338

339

340

341

342

343

344

345

346

Figure 9. Deconvolution model estimates for the precession index wave (blue curve), obliquity wave (red curve), and their sum (grey curve with red dots) associated with the percentage change between successive mean-daily-insolation maxima and minima at 65N latitude during June from -844,200 to +53,500 years (IMCCE, 2018).

The values greater or less than zero represent increasing or decreasing changes from each contribution to successive mean-daily-insolation extrema transitions. They, therefore, provide systematic trends associated with mean daily insolation changes over time, which are not evident in Figure 7. These increasing and decreasing trends will be shown to correlate with the prominent features in paleoclimate data.

Note that the precession index and obliquity contributions to successive mean-daily-insolation extrema from equations (4), (6), (8), and (9) contribute to the neglected cross-term corrections to equation (3). At best, these corrections are an order of magnitude less than the leading terms, which validates equation (3).



347

348

349

350

351

352

353

354

355

356

357

358

359

360

361

362

363

364

365

366

367

368

369

370

371

372

373

374

375

376

377

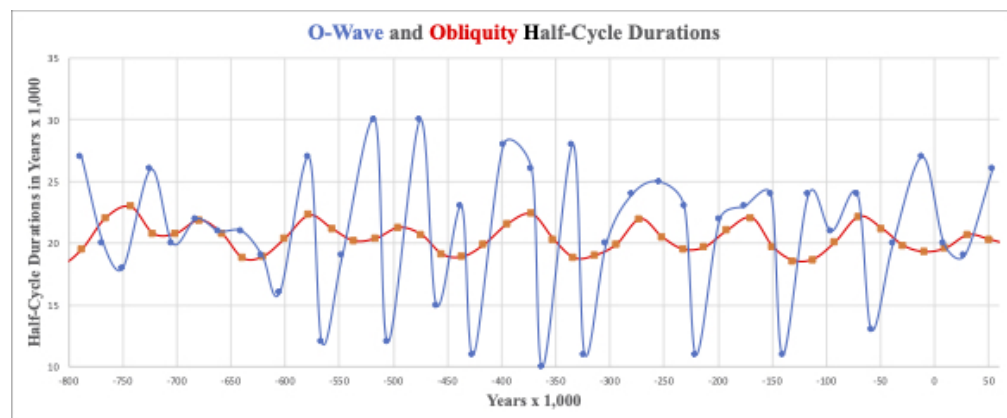
The three curves in Figure 9 are based on best fits to a sparse set of points. Therefore, they cannot be trusted for numerical accuracy between the indicated grey, blue, and red points. Nevertheless, the curves provide qualitative features and quantitative estimates as well as a conceptual language involving waves that will be exploited below to physically describe the prominent features of the EDC ice core data of Figure 1.

The obliquity contribution (red curve) in Figure 9 will be referred to as the O-Wave. It appears as an oscillatory wave of varying half-cycle duration having a narrowly bound amplitude. Its contributions range from about 6% (-219,600 years) to -5% (-115,700 years).

The precession index contribution (blue curve) will be referred to as the PI-Wave of recurring wave packets comprised of a precession carrier wave modulated by an eccentricity wave. It's contribution ranges from about 21% (-219,600 years) to -18% (-208,700 years). Note that the eccentricity's primary effect amplifies and reduces the insolation in a quasiperiodic manner through the recurring PI wave packets.

Finally, the grey curve is the sum of the O-Wave and PI-Wave contributions. Note the O-Wave enhances and diminishes the PI-Wave contribution to the grey curve primarily at its maxima and minima (red dots) in Figure 9. These points and the insolation trends represented by the PI-Wave will play a role in correlating the model predictions with prominent features of the EDC data.

While the magnitudes of the O-Wave maxima are mostly smaller (a factor of four smaller in some cases) than that of the PI-Wave, its half-cycle duration is on average a factor of two greater than that of the precession carrier wave. However, O-Wave half-cycle durations can only be crudely estimated because of the sparse set of points. Nevertheless, the O-Wave varies slowly compared to the precession carrier wave with approximate half-cycle durations that range from about 10,000 to 30,000 years (21,000 years on average), which differ significantly from the obliquity half-cycle durations, as indicated in Figure 10,



378

379

380

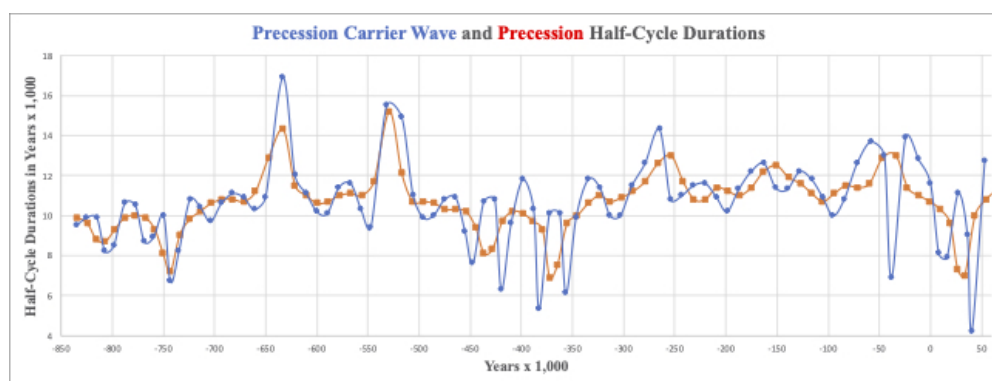
Figure 10. A comparison of O-Wave half-cycle durations inferred from the deconvolution model with obliquity half-cycle durations calculated during the period -787,500 years to +54,000 years (IMCCE, 2018).



381 Note the similar behavior of the O-Wave (blue curve) to the far-left and far-right, which will be  
 382 discussed further in Section V regarding the Holocene termination.

383

384 In Figure 9, the PI-Wave contributions (blue curve) to the mean-daily-insolation extrema  
 385 transitions are analogous to an AM radio wave having approximate carrier wave half-cycle  
 386 durations ranging from about 4,000 to 17,000 years (11,000 years on average). In Figure 11, this  
 387 range (blue curve) differs from the precession half-cycle durations (red curve),  
 388



389

390 Figure 11. A comparison of precession carrier wave half-cycle durations (blue curve) inferred from the  
 391 deconvolution model with the precession half-cycle durations (red curve) determined during the period -844,200  
 392 years to +54,200 years (IMCCE, 2018).

393

394 Due to the sparse set of points available from the deconvolution model and multiple and  
 395 variable half-cycle durations, a graphical analysis is adopted in the next section to establish  
 396 correlations between the estimated PI-Wave and O-Wave contributions to successive insolation  
 397 extrema transitions and the EDC data.

398

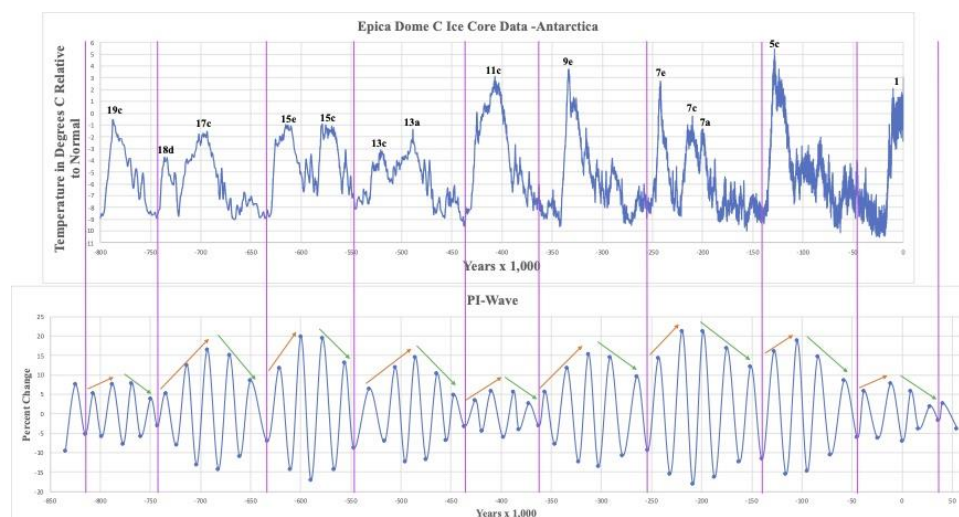
#### 399 IV. Climate History Correlations

400

401 Because of the earth's highly complex climate system and unknown conditions in the  
 402 past, its response to external effects such as celestial mechanical forcing is very challenging to  
 403 predict. Adding to this complexity are internal effects within the earth system that can also affect  
 404 its climate, such as volcanic eruptions, albedo changes, etc. Hence, the detailed behavior of the  
 405 earth's climate between and during interglacial periods is far beyond the scope of this paper.  
 406 Nevertheless, the predictions from the deconvolution model will be used to interpret the EDC  
 407 data. This semi-quantitative approach indicates that there are correlations between celestial  
 408 mechanical forcing and prominent features in the data.

409

410 Consider the comparison of Figure 1 EDC data modified by Marine Isotope Stage (MIS)  
 411 designations (Berger et al., 2015) with the PI-Wave of Figure 9 is represented in Figure 12,

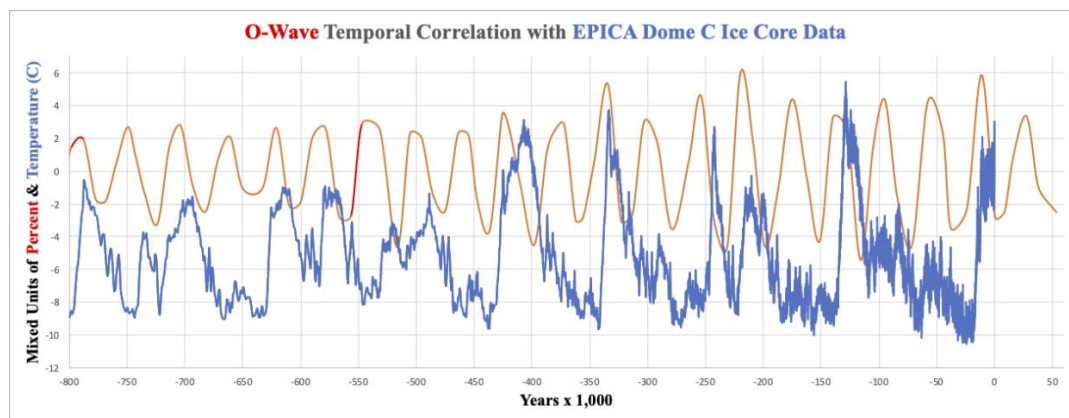


412  
 413 Figure 12. PI recurring wave packets (judiciously defined by purple vertical lines) approximately correlate with  
 414 interglacial and glacial periods over the last 800,000 years. Precession carrier wave maxima trends qualitatively  
 415 correlate with increasing temperature trends (red arrows) and decreasing maxima trends (green arrows) with  
 416 decreasing temperature.

417  
 418 Visually, the quasiperiodic PI wave packets, which are specified by the vertical purple lines,  
 419 roughly correlate with recurring interglacial and glacial periods. To determine occurrences of  
 420 interglacial and glacial periods, simply follow the recurring PI wave packets. However, the  
 421 relationship between the timing of prominent temperature excursions and deconvolution model  
 422 predictions also depends on the O-Wave contributions (see further discussion below).  
 423 Nevertheless, increasing temperatures in the EDC data coincide with increasing precession  
 424 carrier wave maxima (red arrows), while declining temperature trends follow the decreasing  
 425 trend in precession carrier wave maxima (green arrows). These trends in amplitudes are  
 426 primarily due to eccentricity changes. The eccentricity during precession carrier wave cycles  
 427 amplifies and reduces the insolation over substantial periods, which roughly correlate with the  
 428 initiation and termination of interglacial periods.

429  
 430 Note that some temperature trends are interrupted by precession carrier wave amplitude  
 431 reductions that appear to “split” the temperature peaks into MIS pairs, namely, 18d-17c,  
 432 15e-15c, 13c-13a, 7e-7c, and 7c-7a (see further discussion below). Also, note the similarity in Figure 12  
 433 between the wave packet to the far left (associated with MIS 19c) and the last one to the far right  
 434 (associated with MIS 1), which is the Holocene, but more about this relationship later.

435  
 436 The O-Wave contribution to the percentage change of successive mean-daily-insolation  
 437 extrema at 65N during June also qualitatively correlates with EDC temperature excursions as  
 438 indicated in Figure 13,  
 439



440

441

442

443

444

Figure 13. O-Wave predictions from the deconvolution model and EDC data indicate a qualitative temporal correlation between O-Wave maxima and EDC temperature peaks. The O-Wave curve is constructed from 85 data points while the EDC data involves 5,788 points.

445

446

447

448

449

450

451

452

453

454

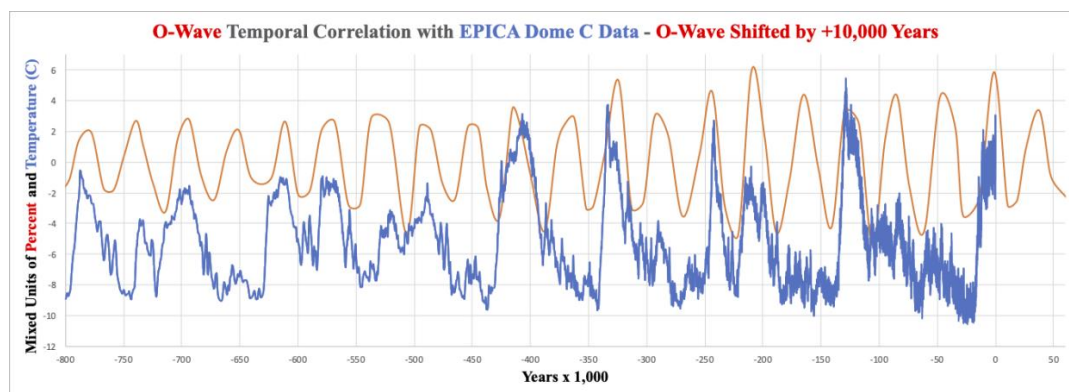
455

456

457

The comparison in Figure 13 indicates that both data sets have similar quasiperiodic behaviors with the O-Wave systematically lagging the EDC data (see discussion below). It also indicates that there were 20 O-Wave maxima and 13 prominent temperature excursions with numerous temperature “bumps” in between over the last 800,000 years. Also note that from -430,000 years to the present, the obliquity wave maxima tend to be higher, and the minima lower than the period -800,000 to -430,000 years. This behavior may, in part, account for the systematically higher and lower temperatures during the period -430,000 years to present compared to the earlier period often referred to as the mid-Brunhes Climate Transition.

The temporal correlation between the O-Wave oscillations and EDC temperature excursions can be qualitatively improved by shifting O-Wave data by +10,000 years as indicated in Figure 14,



458

459

460

461

Figure 14. O-Wave predictions from deconvolution model and EDC data with the O-Wave temporally shifted by +10,000 years indicating an improved qualitative correlation between O-Wave maxima and EDC temperature peaks.



462 Note, the 10,000-year shift is comparable to the average precession carrier wave half-cycle  
463 duration. In what follows, the timing differences between the O-Wave contribution and the  
464 temperature excursions are ameliorated through interference between the PI- and O-Wave.

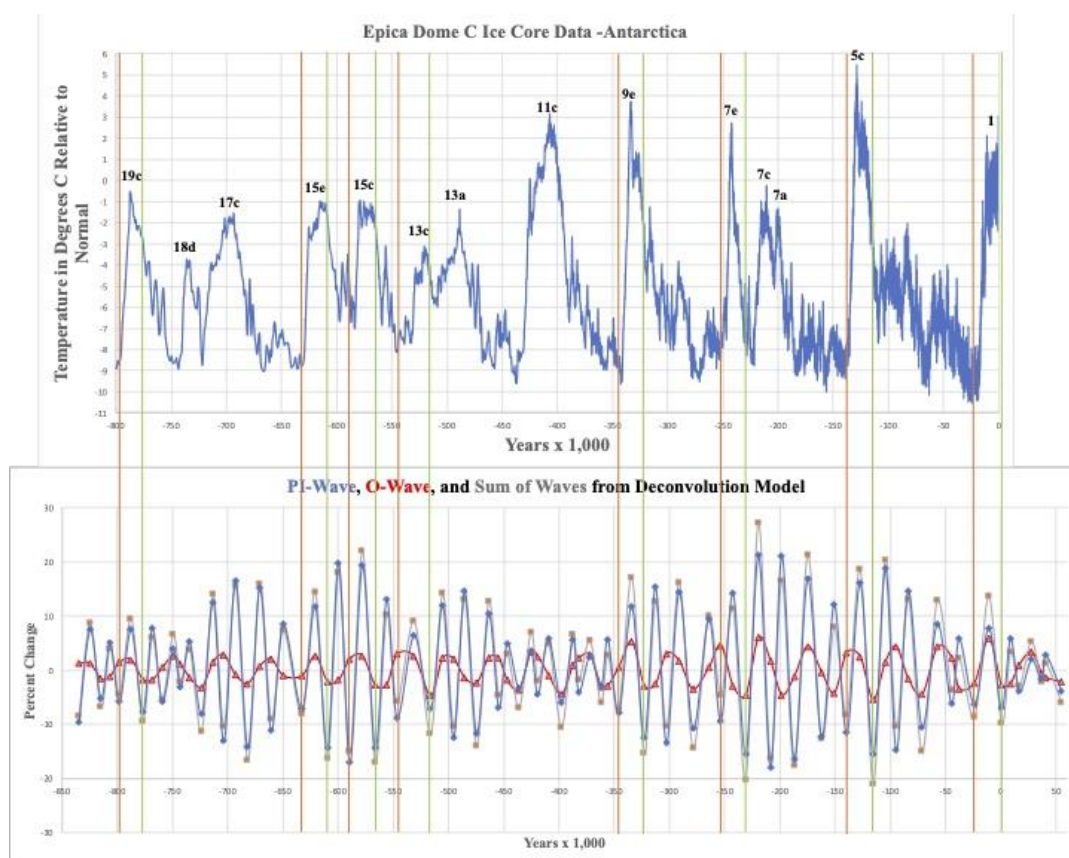
465

466 Utilizing the above wave taxonomy, interglacial periods can be classified into two types.  
467 Those of Type I occur over one precession carrier wave cycle. During such a cycle, there is an  
468 approximate constructive interference between the precession carrier and O waves. Those of  
469 Type II occur over two precession carrier cycles; however, there is constructive and destructive  
470 interference between the precession carrier and O waves during such cycles.

471

472 Using MIS designations, those of Type I are 19c, 15e, 15c, 13c, 9e, 7e, 5e, and 1, which  
473 are represented in Figure 15,

474



475

476 Figure 15. Type I interglacial initiations (red vertical lines) are followed by interglacial terminations (green vertical  
477 lines). Initiations coincide with concurrent PI-Wave, and O-Wave increases to the right of the red vertical lines, and  
478 terminations coincide with corresponding concurrent declines ending in green vertical lines.

479

480 Each pair of vertical red and green lines extending across both graphs relates the duration of each  
481 precession carrier cycle and its corresponding MIS interglacial. For Type I, all PI-Wave  
482 contributions constructively interfere with O-Wave contributions except for MIS 7e (see further



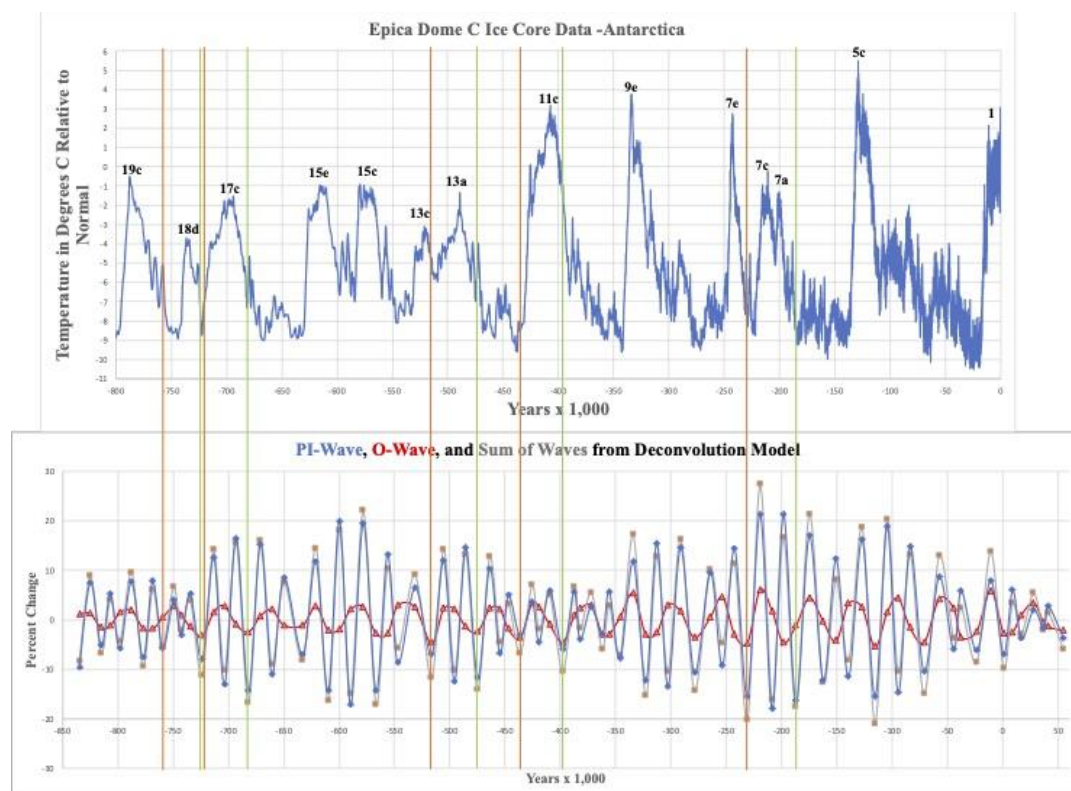
483 discussion below). Starting from the right of each vertical red line, both contributions  
484 concurrently increase to approximately synchronized maxima associated with the red dots of the  
485 grey curve and then decline concurrently to the vertical green lines terminating on the red dots of  
486 gray curve minima. The vertical green lines define all interglacial terminations, which are  
487 comparatively sharp. Note the role of the O-Wave is to enhance (constructive interference) the  
488 precession carrier wave maxima and minima as indicated by the red dots associated with grey  
489 curve maxima (excluding for MIS 7e) and minima (including MIS 7e). The termination of MIS  
490 1, the Holocene, will be discussed in the next section.

491  
492 For MIS 7e, the PI- and O-Wave contributions are initially out of phase by about  $\frac{1}{4}$  of an  
493 O-Wave cycle; however, they partially constructively interfere as the PI-Wave contribution  
494 increases to the right of the indicated vertical red line. The duration of this interglacial is likely  
495 cut short because the O-Wave contribution subsequently destructively interferes with the PI-  
496 Wave contribution. However, MIS 7e terminates like all others of Type I as indicated by the  
497 deep minimum at the green line (the grey curve red dot minimum).

498  
499 Note also, the delay in the initiation of interglacial MIS 13c, which has the longest  
500 precession carrier wave cyclical duration of about 30,000 years. Its precession carrier wave  
501 maximum represents a decline from the earlier maximum in Figure 15. Note the O-wave  
502 contribution is out of synchronization, which broadens the insolation maximum. Also, the  
503 amplification rate of the insolation during this period is comparatively low due to its long  
504 duration. This delay is described further below, along with another initiation delay associated  
505 with a Type II interglacial.

506  
507 The interglacial periods of Type II are MIS 18d, 17c, 13a, 11c, and 7c-7a. The latter  
508 hyphenated designation is further explained below. Each of these periods involves a pair of  
509 precession carrier wave maxima trending higher, as depicted in Figure 16,  
510





511  
 512 Figure 16. Type II interglacial initiations (red vertical lines) are followed by interglacial terminations (green vertical  
 513 lines). Initiations coincide with concurrent PI-Wave and O-Wave increases to the right of the red vertical lines,  
 514 while terminations coincide with in phase PI-Wave and O-Wave minima that coincide with corresponding green  
 515 vertical lines. Note that the pair of green and red lines associated with the MIS 18d-17c split the interglacial.

516  
 517 Again, the pair of vertical red and green lines identify the temporal extent of two precession  
 518 carrier wave maxima and minima and their corresponding interglacial period. The O-Wave  
 519 contributions occur over a longer half-cycle than the Type I set. In all cases, an O-Wave  
 520 maximum is approximately in phase with the first precession carrier wave maximum  
 521 (constructive interference). The O-Wave is then out of phase with the next precession carrier  
 522 wave minimum and maximum (destructive interference). Eventually, the O-Wave contribution  
 523 ends approximately in phase with the final precession carrier wave minimum except for MIS 7c-  
 524 7a, which is about ¼ of an obliquity wave cycle out of phase (about 11,000 years). However, in  
 525 the latter case, the O-Wave contribution is negative at the second precession carrier wave  
 526 minimum, so it constructively contributes to the MIS 7a termination as indicated by the deep  
 527 minimum at its green vertical line (red dot minimum of the grey curve).  
 528

529 MIS 7c-7a appears to be an interglacial that is split in two. It is associated with  
 530 successive precession carrier wave maxima and minima that have the largest magnitudes over  
 531 the last 800,000 years. There is a concurrent decline in the precession carrier wave and O-Wave  
 532 contributions between the precession carrier wave peaks. The timing of this concurrent decline  
 533 likely accounts for the split in the MIS 7c-7a interglacial. However, the MIS 7a temperature peak



534 is of a very short duration, likely due to the destructive interference between the second  
535 precession carrier wave peak and the O-Wave. Note that MIS pairs 18d-17c, 15e-15c, 13c-13a,  
536 and 7e-7c also appear to be split by PI- and O-Wave cyclical behaviors.

537

538 All Type I and II interglacial durations are approximately determined by their precession  
539 carrier wave durations. However, there are delays in the initiation of MIS 18d (5,000–7,000  
540 years) and MIS 13c (11,000–13,000 years). For MIS 18d, the precession carrier wave maximum  
541 to the right of the red line is a part of an insolation decline despite its enhancement from the O-  
542 Wave contribution (red dot on grey curve). The subsequent second precession carrier wave  
543 maximum (MIS 18d is of Type II) is even less by about 2%. This feature may account for the  
544 comparatively small MIS 18d temperature excursion. The relatively low rate of increasing  
545 insolation may also account for the comparatively small MIS 13c temperature excursion.

546

547 Both MIS 18d and 13c also represent deep ice cores (time is a function of core depth),  
548 where physical effects can affect the estimated time of these interglacial inceptions and  
549 terminations using ice core models. It has been noted (Parrenin et al., 2007) that the most  
550 significant timing discrepancies between paleoclimate datasets EDC and LR04 benthic  $\delta^{18}\text{O}$   
551 occur for MIS 18d and 13c. This comparison suggests that the deconvolution model predictions  
552 for the timing of interglacial initiations and terminations could be correct and that another  
553 examination of the EDC data may resolve the timing discrepancies between the deconvolution  
554 predictions presented here and the data.

555

556 Overall, the rates of insolation amplification as indicated by the recurring PI wave  
557 packets (enhanced by the obliquity contribution) appear to correlate with rising EDC temperature  
558 excursions. Similarly, the rates of insolation decline represented by the recurring PI wave  
559 packets (reduced by the O-Wave contribution) correlate with persistent temperature declines. All  
560 interglacial terminations coincide with the same celestial mechanical forcing conditions.

561

## 562 **V. Estimating the Holocene Termination**

563

564 The analysis presented above indicates that MIS 1 is a Type I interglacial. As such, it is  
565 expected to terminate because of PI- and O-Wave constructive interference. The MIS 1 one cycle  
566 classification indicates that MIS 11c is an unlikely analog, which has been proposed in the  
567 literature (Berger et al., 2003).

568

569 MIS 19c has also been identified as a possible Holocene analog based solely on the  
570 behavior of celestial parameters and comparable mean-daily-insolation changes (Vavrus et al.,  
571 2018). The analysis presented below addresses the similarities and differences between MIS 19c  
572 and MIS 1 based on PI- and O-Wave contributions to the percentage change between successive  
573 mean-daily-insolation extrema at 65N latitude during June.

574

575 As pointed out earlier in Figure 10, the O-Wave half-cycle durations of MIS 19c and MIS  
576 1 are similar. They both are associated with an O-Wave cycle duration of about 37,000 years,  
577 with approximate half-cycles of 27,000 years on the upside and 10,000 years on the downside.  
578 They also have comparable declines in mean-daily-insolation from their maxima to minima. For  
579 MIS 19c, the decline is about 48 Watts/m<sup>2</sup> while for MIS 1, it's about 50 Watts/m<sup>2</sup>.



580

581

582 Their main difference is the estimated duration of their precession carrier wave cycle and

583 half-cycle durations. For MIS 19c, the precession carrier wave cycle duration is about 21,000

584 years, while for MIS 1, it's about 24,000 years. This difference indicates that MIS 1 will likely

585 be a longer interglacial than MIS 19c. In terms of interglacial terminations, the MIS 19c

586 downside precession carrier wave half-cycle duration is about 10,500 years, while for MIS 1, it is

587 about 11,600 years.

588

589 In Figures 15 and 16, Type I and II terminations end on grey curve red dot minima that

590 involve O-Wave enhancements (constructive interference) to precession carrier wave minima.

591 The following table summarizes the termination estimates for each MIS based on their downside

592 precession carrier wave half-cycle duration,

592

Type I	MIS #	Termination (years)
	19c	10,500
	15e	11,100
	15a	11,700
	13c	14,800
	9c	11,400
	7e	11,500
	5e	11,800
	1	11,600
Type II	18d	10,800
	17c	11,100
	13a	10,800
	11c	11,800
	7c-7a	11,200

593

594

595

596

597

598

599

600

601

602

603

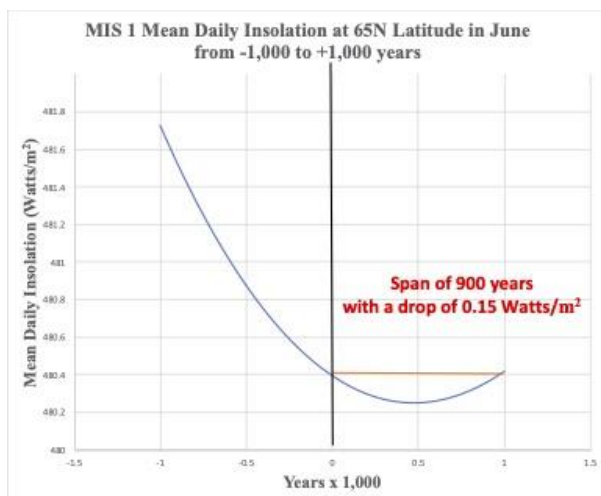
604

605

Table I. MIS termination duration estimates based on the last precession carrier wave peak to the vertical green line in Figures 15 and 16.

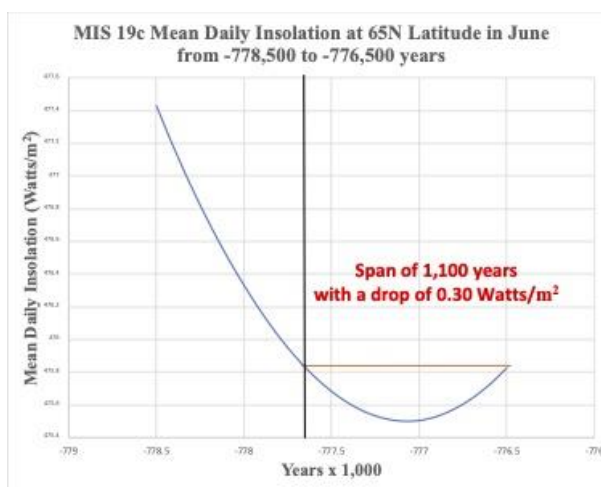
These termination estimates are all comparable (within hundreds of years of each other) in duration except for MIS 13c, which has the longest cyclical duration and the largest downside precession carrier wave half-cycle duration of 14,800 years.

Assuming the vertical green line for MIS 1 in Figure 15 is accurate, its termination will occur within about 500 years from the present; however, exactly when cannot be determined just from celestial mechanical forcing. This estimate coincides with the local minimum in insolation using Laskar's tool as indicated in Figure 17,



606  
607 Figure 17. MIS 1 mean-daily- insolation at 65N latitude during June  
608 from -1,000 to +1,000 years. The shallow minimum at +500 years  
609 measured from the vertical black line estimates the Holocene  
610 termination, which coincides with the vertical green line in Figure 15.  
611

612 This estimate is of low resolution because the above minimum is very shallow. The earth will  
613 remain in this shallow minimum for at least 900 years. MIS 19c shares the same feature as  
614 indicated in Figure 18,  
615

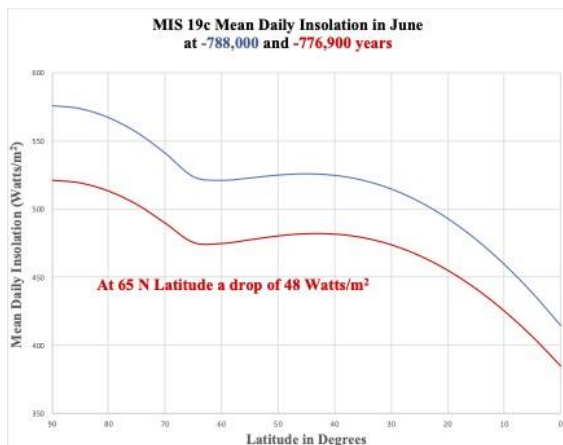


616  
617 Figure 18. MIS 19c mean-daily-insolation at 65N latitude during June  
618 from -778,500 to -776,500 years. The shallow minimum at 600 years  
619 measured from the vertical black line is a termination estimate that  
620 coincides with the vertical green line in Figure 15.  
621

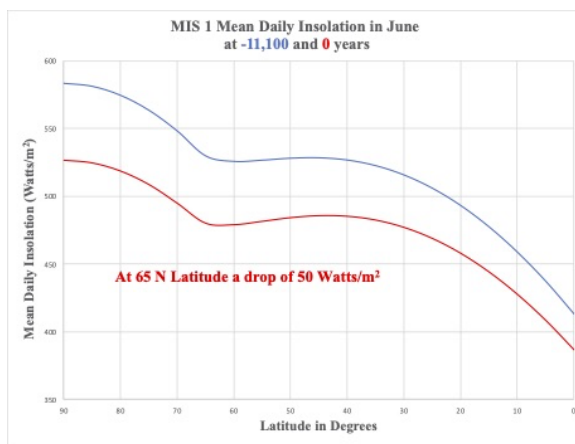
622 , which also has a relatively shallow minimum over 1,100 years. Note that all other interglacial  
623 terminations share this common feature.  
624



625           Given the consistent recurrence of the interglacial terminations based on celestial  
626 mechanical forcing over the last 800,000 years, it is likely that there is a common physical  
627 mechanism that accounts for interglacial terminations. Milankovitch Theory focuses on northern  
628 latitudes at or greater than 65N because of the potential for ice sheet growth due to the decline in  
629 mean-daily-insolation at these latitudes during June over thousands of years. The substantial  
630 reduction in the mean-daily-insolation over 11,100 years for the Holocene has likely had a  
631 cooling effect on the air over a range of latitudes. This latitudinal range is due to a tradeoff  
632 between increasing insolation as the latitude decreases (the obliquity has decreased over the last  
633 11,100 years) along with a concurrent decline in daylight hours. As examples, Figures 19 and 20  
634 demonstrate the extensive nature of this latitudinal effect for MIS 19c and 1,  
635



636  
637 Figure 19. Latitudinal effect on mean-daily-insolation over a  
638 period of 11,100 years for MIS 19c (IMCCE, 2018).  
639



640  
641 Figure 20. Latitudinal effect on mean-daily-insolation over a  
642 period of 11,100 years for MIS 1 (IMCCE, 2018).  
643

644 This gradual reduction in mean-daily-insolation during June over the last 11,100 years enables  
645 air at northern latitudes to more readily cool during the winter solstice (the hour angle



646 significantly decreases), which has the potential to increase the dense cold air volume at northern  
647 latitudes. Similar insolation reductions have occurred many times over the last 800,000 years;  
648 however, the specific physical mechanism in the earth's climate that couples to such insolation  
649 reductions to cause a temperature descent into a glacial remains unknown. It is therefore  
650 impossible to predict the consequences of this insolation condition on the earth's climate in  
651 detail. Our understanding of the earth's climate is still not good enough. Nevertheless, the  
652 insolation condition consistently coincides with quasi-periodic temperature declines associated  
653 with ice ages.

654

655 In recent times, the cold air volume above 60N latitude has produced extreme weather  
656 events associated with an instability of the polar vortex - stable cold, dense air counter-rotating at  
657 northern latitudes - that is kept in check by the jet stream. The specific conditions that produce  
658 these events are not well understood due to the lack of a reliable theory of the earth's climate. At  
659 best, there are models (Lawrence et al., 2020) that attribute different physical mechanisms to  
660 these events. However, the recurrence of such events over an extended period can result in ice  
661 and snow accumulation that can change the earth's albedo, producing cooler climates because of  
662 gradual changes in the earth's heat engine.

663

664 It's essential to keep in mind that the above estimated MIS 1 termination is tentative.  
665 Nevertheless, based solely on celestial mechanical forcing, the Holocene termination is likely to  
666 happen as all other interglacial terminations over the last 800,000 years.

667

## 668 **VI. Summary**

669

670 The deconvolution model presented here provides additional insight into the roles of the  
671 precession index and obliquity contributions to the insolation. In particular, the recurrence of  
672 interglacial and glacial periods over the last 800,000 years approximately correlates with the  
673 quasiperiodic behavior of PI wave packets. This correlation is reinforced by the quasiperiodic  
674 behavior of the O-Wave contribution to the insolation. In addition, all interglacial inceptions and  
675 terminations involve constructive interference between the PI and O waves. Finally, interglacial  
676 durations roughly coincide with the number and duration of precession carrier wave cycles.  
677 These new results support Milankovitch Theory.

678

679 Based solely on celestial mechanical considerations, the estimated Holocene termination  
680 will occur within the next 500 years. This estimated range is due to the shallow insolation  
681 minimum that will persist for the next 900 years as indicated in Figure 17. The estimated  
682 duration of the glacial period that will follow this termination is about 36,000 years based upon  
683 the temporal duration of the precession index wave packet of Figure 15. After this period, there  
684 will be another increase in temperature, but the magnitude cannot be determined.

685

686 However, the comparison between the model predictions and EDC data indicates two  
687 timing inconsistencies. There are delays in interglacial inceptions associated with MIS 18d and  
688 13c; however, these may be due to physical effects related to deep ice cores. Nevertheless, the  
689 roles of the PI and O waves predicted by the deconvolution model should motivate further  
690 examination of paleoclimate data tuning. In this regard, further progress on improving estimates



691 of O-Wave cyclical durations would likely enhance the time calibration of the observed features  
692 in paleoclimate data.

693

694 Finally, given the recurrent PI- and O-Wave pattern associated with interglacial  
695 terminations, the search for a common physical mechanism related to the earth's future climate  
696 becomes more compelling. It is likely that a cumulative effect occurs over an extended period  
697 (the next 500 years) that eventually tips the earth into a persistent temperature descent concurrent  
698 with the decline in precession carrier wave maxima. This trend very likely impairs recovery  
699 until there is a return to increasing precession carrier wave maxima as Figure 12 indicates.  
700 Identifying the specific physical mechanism that causes this descent is far beyond the scope of  
701 this paper. Nevertheless, the potential expansion of the cold air volume at northern latitudes due  
702 to significant declines in insolation over the last 11,100 years should be investigated as a possible  
703 cause. Given recurring PI wave packets and their correlation with interglacial and glacial periods  
704 over the last 800,000 years, the catastrophic consequences to the future of civilization from  
705 another ice age should provide ample motivation to intensify scientific research in this vitally  
706 important area for all of humanity.

707

#### 708 **Acknowledgments**

709

710 I would like to acknowledge numerous exchanges with Professor William H. Smith of  
711 Washington University, St. Louis, concerning Milankovitch Theory. I would especially like to  
712 thank Dr. Patrick Frank and Patrice Poyet for reading the manuscript and making numerous  
713 helpful suggestions that measurably improved the clarity and presentation of the results. I am  
714 also indebted to Bruce Bauer, Data Manager, World Data Service for Paleoclimatology and  
715 NOAA National Centers for Environmental Information (NCEI) Climatic Science and Services  
716 Division – Paleoclimatology Boulder, CO for providing the relevant paleoclimate datasets.  
717 Finally, I would like to express my gratitude to Dr. Jacques Laskar for directing me to the  
718 wonderful computational tool he and his colleagues created, which enabled all the computations  
719 in this paper.

720

#### 721 **Appendix A**

722

723 This section aims to derive equations (8) and (9) using light rays and vector analysis. The  
724 sun's light rays hit the earth with uniform intensity at angles relative to tangential planes over the  
725 earth's surface. However, there is a point on the earth where the rays are perpendicular to a  
726 tangential plane, the subsolar point. As the earth rotates, this point moves westward and north  
727 and south due to the earth's obliquity and orbit in a wavelike pattern completing an entire cycle  
728 over a year.

729

730 For an observer at a point on the earth looking vertically, there is a component of a solar  
731 ray parallel to the vertical and another tangential. The vertical component is of interest in  
732 determining the obliquity contribution to the insolation, while the tangential component is  
733 assumed lost. The key quantity to determine is the time-dependent zenith angle between an  
734 observer vector pointing vertically and the declination vector pointing from the earth's center to  
735 the subsolar point. The deconvolution model assumes that the cosine of this angle times an  
736 overall constant determines the obliquity contribution to the insolation. Because the observer

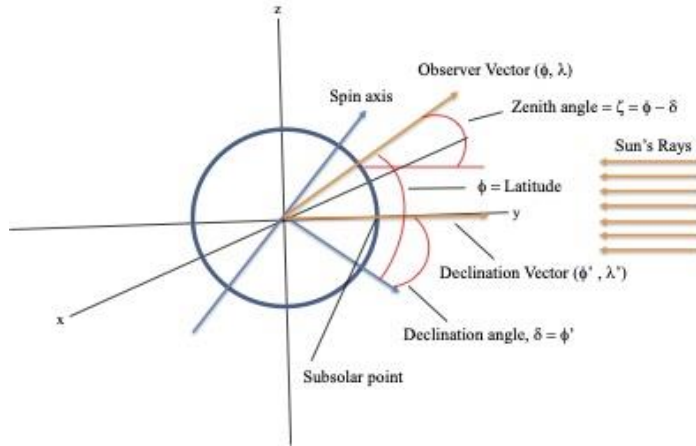


737 and subsolar point move relative to the sun, the mean daily insolation is the average of the cosine  
 738 of the zenith angle over daylight hours.

739

740 The relevant angles and vectors defined with respect to the earth's body fixed rotating  
 741 axes are represented in the following diagram,

742



743

744

745

746

747

**Figure 1A.** A diagram that defines the relevant vectors of the observer and declination in terms of their latitudes and longitudes,  $(\phi, \lambda)$  and  $(\phi' = \delta, \lambda')$ , respectively defined with respect to rotating body fixed axes. The observer latitude and the declination angle,  $\delta$ , determine the zenith angle,  $\zeta$ .

748

The observer unit vector in the rotating body-fixed frame is given by,

749

$$750 \vec{V}_o = \cos(\phi) \cdot \cos(\lambda) \vec{i} + \sin(\phi) \cdot \cos(\lambda) \vec{j} + \sin(\lambda) \vec{k} \quad (1A)$$

751

, and the declination unit vector is given by,

752

$$754 \vec{V}_\delta = \cos(\phi') \cdot \cos(\lambda') \vec{i} + \sin(\phi') \cdot \cos(\lambda') \vec{j} + \sin(\lambda') \vec{k} \quad (2A)$$

755

756 , where  $\phi' = \delta$ , the declination angle. The cosine of the zenith angle is simply the scalar product  
 757 of equations (1A) and (2A) given by,

758

$$759 \vec{V}_o \cdot \vec{V}_\delta = \cos(\zeta) = \sin(\phi) \cdot \sin(\delta) + \cos(\phi) \cdot \cos(\delta) \cdot \cos(h) \quad (3A)$$

760

761 , where  $h = \lambda' - \lambda$  is the hour angle, which for sunrise and sunset is determined by  $\cos(\zeta) = 0$   
 762 or

763

$$764 h_0 = \cos^{-1}(-\tan(\phi) \cdot \tan(\delta)) \quad (4A)$$

765

766 , which equals equation (9) for the summer solstice when  $\delta = \theta$ , the earth's obliquity angle.

767

768

769 For the deconvolution model, we assume the obliquity contribution to the insolation during the summer solstice is of the form





770

$$771 \quad B = G \cdot (\sin(\phi) \cdot \sin(\theta) + \cos(\phi) \cdot \cos(\theta) \cdot \cos(h)) \quad (5A)$$

772

773 , where  $G$  is an overall constant. The mean daily obliquity contribution to the mean daily  
774 insolation,  $\bar{Q}$ , of equation (2) is obtained by averaging equation (5A) over daylight hours given  
775 by

776

$$777 \quad \bar{B} = \frac{G}{2 \cdot \pi} \cdot \int_{-h_0}^{h_0} (\sin(\phi) \cdot \sin(\theta) + \cos(\phi) \cdot \cos(\theta) \cdot \cos(h)) \, dh \quad (6A)$$

778

$$779 \quad = \frac{G}{\pi} \cdot (h_0 \cdot \sin(\phi) \cdot \sin(\theta) + \cos(\phi) \cdot \cos(\theta) \cdot \sin(h_0)) \quad (7A)$$

780

781 , from which equation (8) follows straightforwardly with  $h_0$  determined by equation (4A) with  
782  $\delta = \theta$ .

783

## 784 **References**

785

786 Berger, A., Loutre, M.F. and Crucifix M., The Earth's Climate in the Next Hundred Thousand  
787 Years (100 kyr), *Surv. Geophys.*, Vol. 24, pp. 117–138,  
788 <https://link.springer.com/article/10.1023/A:1023233702670>, 2003.

789

790 Berger, A., Crucifix, M., Hodell, D.A, Mangili, C., McManus, J.F., Otto-Bliesner, B., Pol, K.,  
791 Raynaud, D., Skinner, L.C., Tzedakis, P.C., Wolff, E.W., Yin, Q.Z., Abe-Ouchi, A., Barbante,  
792 C., Brovkin, V., Cacho, I., Capron, E., Ferretti, P., Ganopolski, A., Grimalt, J.O., Hönisch, B.,  
793 Kawamura, K., Landais, A., Margari, V., Martrat, B., Masson-Delmotte, V., Mokeddem, Z.,  
794 Parrenin, F., Prokopenko, A.A., Rashid, H., Schulz, M., and Vazquez Riveiros, N., Interglacials  
795 of the Last 800,000 Years, *Rev. Geophys.*, Review Article, pp. 1-58,  
796 <https://agupubs.onlinelibrary.wiley.com/doi/full/10.1002/2015RG000482>, 2015.

797

798 Berger, W.H., Milankovitch Theory - Hits and Misses, Scripps Institution of Oceanography,  
799 Technical Report, pp. 1-35, <https://escholarship.org/uc/item/95m6h5b9>, 2012.

800

801 Gradstein, F., Ogg, J., and Smith, A., A Geologic Time Scale 2004, Cambridge University Press,  
802 Book, pp. 1-589, [https://www.cambridge.org/core/books/geologic-time-scale-  
2004/ACED6139A9320FC9CA982E316FFF3E38](https://www.cambridge.org/core/books/geologic-time-scale-2004/ACED6139A9320FC9CA982E316FFF3E38), 2005.

803

804  
805 Hays, J.D., Imbrie, John, and Shackleton, N.J., Variations in the Earth's Orbit: Pacemaker of the  
806 Ice Ages, *Science*, Vol. 194 (4270): pp. 1121–1132,  
807 <https://www.science.org/doi/10.1126/science.194.4270.1121>, 1976.

808

809 Huybers, P., Combined Obliquity and Precession Pacing of Late Pleistocene \Deglaciations,  
810 *Nature*, Vol. 480, pp. 229–232, <https://www.nature.com/articles/nature10626>, 2011.

811

812 Imbrie, J., Astronomical Theory of the Pleistocene Ice Ages, *Icarus*, Vol. 50 (2-3), pp. 408-422,  
813 <https://www.sciencedirect.com/science/article/abs/pii/0019103582901324>, 1982.



- 814  
815 Imbrie, J., and Imbrie, K. P., Ice Ages: Solving the Mystery, Harvard University Press, Book,  
816 pp.1-224, <https://www.hup.harvard.edu/catalog.php?isbn=9780674440753>, 1986.  
817  
818 IMCCE, Virtual Observatory Solar System Portal, CNRS Observatory, Paris,  
819 <http://vo.imcce.fr/insola/earth/online/earth/online/index.php>, 2018. Numerical calculations in this  
820 paper make considerable use of data generated from this computational tool.  
821  
822 Jouzel, J., A Brief History of Ice Core Science over the Last 50 Years, *Clim. Past*, Vol. 9, pp.  
823 2525-2547, <https://cp.copernicus.org/articles/9/2525/2013/>, 2013.  
824  
825 Laskar, J., Robutel, P., Joutel, F., Gastineau M., Correia, A.C.M., and Levrard, B., A Long-Term  
826 Numerical Solution for the Insolation Quantities of the Earth,  
827 *Astron. Astrophys.*, Vol. 428, pp. 261-285,  
828 <https://www.aanda.org/articles/aa/full/2004/46/aa1335/aa1335.html>, 2004.  
829  
830 Lawrence, Z.D., Perlwitz, J., Butler, A.H., Manney, G.L., Newman, P.A., Lee, S.H., and Nash,  
831 E.R., The Remarkably Strong Arctic Stratospheric Polar Vortex of Winter 2020: Links to Record  
832 Breaking Arctic Oscillation and Ozone Loss, *J. Geophys. Res.-Atmos.*, Vol. 125, pp. 1-21,  
833 <https://doi.org/10.1029/2020JD034190>, 2020.  
834  
835 Lisiecki, LE. and Raymo, M.E., A Pliocene-Pleistocene Stack of 57 Distributed Benthic  $\delta^{18}\text{O}$   
836 Records, *AGU Paleoclimatology and Paleoclimatology*, Vol. 20 (PA1003), pp.1-17,  
837 <https://agupubs.onlinelibrary.wiley.com/doi/epdf/10.1029/2004PA001071>, 2005.  
838  
839 Lisiecki, L., Links between Eccentricity Forcing and the 100,000-Year Glacial Cycle, *Nature*  
840 *Geoscience*, Vol. 3, pp. 349–352, <https://www.nature.com/articles/ngeo828>, 2010.  
841  
842 Meyers S.R., Sageman B.B., and Pagani M., Resolving Milankovitch: Consideration of Signal  
843 and Noise, *Am. J. Sci.*, Vol. 308 (6), pp. 770-786, <https://www.ajsonline.org/content/308/6/770>,  
844 2008.  
845  
846 Milankovitch, M., Canon of Insolation and the Ice-Age Problem, *Royal Serb. Acad., Spec. Publ.*,  
847 pp. 1-634, [https://www.amazon.com/Insolation-Ice-Age-Problem-Milankovitch-](https://www.amazon.com/Insolation-Ice-Age-Problem-Milankovitch-Milankovitch/dp/8617066199)  
848 [Milankovitch/dp/8617066199](https://www.amazon.com/Insolation-Ice-Age-Problem-Milankovitch-Milankovitch/dp/8617066199), 1998.  
849  
850 NCEI, EPICA Dome C – 800KYr Deuterium Data and Temperature Estimates,  
851 <https://www.ncei.noaa.gov/access/paleo-search/study/6080>, 2007.  
852  
853 Parrenin, F., Barnola, J.-M. , Beer, J., Blunier, T., Castellano, E., Chappellaz, J., Dreyfus, G.,  
854 Fischer, H., Fujita, S., Jouzel, J., Kawamura, K., Lemieux-Dudon, B., Loulergue, L., Masson-  
855 Delmotte, V., Narcisi, B., Petit, J.-R., Raisbeck, G., Raynaud, D., Ruth, U., Schwander, J.,  
856 Severi, M., Spahni, R., Steffensen, J.P., Svensson, A., Udisti, R., Waelbroeck, C., and Wolff,  
857 E.W., The EDC3 Chronology for the EPICA Dome C Ice Core, *Clim. Past*, Vol. 3, pp. 485-497,  
858 Figure 3, pp. 491, <https://cp.copernicus.org/articles/3/485/2007/>, 2007.



- 859 Roe, G., In defense of Milankovitch, *Geophysical Research Letters*, Vol. 33 (L24703),  
860 <https://agupubs.onlinelibrary.wiley.com/doi/abs/10.1029/2006GL027817>, pp. 1-5, 2006.  
861
- 862 Rohling, E.J., Braun, K., Grant, K., Kucera, M., Roberts, A.P., Siddall, M, Trommer, G.,  
863 Comparison between Holocene and Marine Isotope Stage -11 Sea Level Histories, *Earth Planet.*  
864 *Sc. Letters*, Vol. 291 (1-4), pp. 97–105,  
865 <https://www.sciencedirect.com/science/article/abs/pii/S0012821X1000018X?via%3Dihub>,  
866 2010.  
867
- 868 Vavrus, S.J., He, F., Kutzbach, J.E., Ruddiman, W.F., and Tzedakis, P.C., *Nature: Scientific*  
869 *Reports*, Vol. 8 (10213), pp. 1-12, <https://www.nature.com/articles/s41598-018-28419-5>, 2018.  
870
- 871 Wunsch, C., Quantitative Estimate of the Milankovitch-Forced Contribution to Observed  
872 Quaternary Climate Change, *Quaternary Sci, Rev.*, Vol. 23 (9-10), pp. 1001-1012,  
873 <https://www.sciencedirect.com/science/article/abs/pii/S0277379104000575>, 2004.  
874
- 875 Zachos, J., Pagani, M., Sloan, L., Thomas, E., and Billups, K., Trends, Rhythms, and Aberrations  
876 in Global Climate 65Ma to Present, *Science*, Vol. 292(5517), pp. 686-693,  
877 <https://www.science.org/doi/abs/10.1126/science.1059412>, 2001.  
878  
879